

Nonlinear Optical Imaging of In-Plane Anisotropy in Two-Dimensional SnS

George Miltos Maragkakis, Sotiris Psilodimitrakopoulos, Leonidas Mouchliadis, Abdus Salam Sarkar, Andreas Lemonis, George Kioseoglou, and Emmanuel Stratakis*

Two-dimensional (2D) tin(II) sulfide (SnS) crystals belong to a class of orthorhombic semiconducting materials with remarkable properties, such as in-plane anisotropic optical and electronic response, and multiferroic nature. The 2D SnS crystals exhibit anisotropic response along the in-plane armchair (AC) and zigzag (ZZ) crystallographic directions, offering an additional degree of freedom in manipulating their behavior. Here, advantage of the lack of inversion symmetry of the 2D SnS crystal, that produces second harmonic generation (SHG), is taken to perform polarization-resolved SHG (P-SHG) nonlinear imaging of the in-plane anisotropy. The P-SHG experimental data are fitted with a nonlinear optics model, allowing to calculate the AC/ZZ orientation from every point of the 2D crystal and to map with high resolution the AC/ZZ direction of several 2D SnS flakes belonging in the same field of view. It is found that the P-SHG intensity polar patterns are associated with the crystallographic axes of the flakes and with the relative strength of the second-order nonlinear susceptibility tensor in different directions. Therefore, the method provides quantitative information of the optical in-plane anisotropy of orthorhombic 2D crystals, offering great promise for performance characterization during device operation in the emerging optoelectronic applications of such crystals.

as phosphorene analogues,^[1–4] since they share similar puckered or wavy lattice structures with phosphorene, a 2D format of black phosphorus.^[5,6] The in-plane structural anisotropy of MXs, with puckered structure along the AC direction,^[3] is the origin of in-plane anisotropic physical properties.^[1–3,7,8] A plethora of properties have been reported to exhibit in-plane anisotropic response, including carrier mobility,^[7] optical absorption, reflection, extinction, refraction,^[8] and Raman spectral behavior.^[1] The in-plane anisotropic response is exhibited along the distinguished in-plane AC and ZZ crystallographic directions, offering an additional degree of freedom in manipulating their properties.^[1–3,7,8] For example, polarization-sensitive photodetectors have been presented based on the intrinsic linear dichroism of GeSe,^[8] and black phosphorus.^[9] Furthermore, monolayer MXs are predicted to be multiferroic with coupled ferroelectricity and ferroelasticity, and large spontaneous polarization.^[10,11]

Indeed, in-plane ferroelectricity has been recently demonstrated for micrometer-size monolayer SnS at room temperature.^[12]

Recently, the nonlinear optical properties of MXs have been addressed.^[12–16] Nonlinear optics plays an important role in all aspects of modern photonics, with nonlinear media being used in photonic devices for photon generation, manipulation, transmission, detection and imaging.^[17–20] Applications of nonlinear optics in a wide range of fields have been explored, including nonlinear silicon photonics,^[21] quantum nonlinear optics,^[22] nonlinear plasmonics,^[23] material characterization,^[24–26] and biomedical optics.^[27,28] SHG is possibly the most widely studied nonlinear optical process, in which radiation at twice the frequency of the incident light is generated.^[17–20] It emerges in media that lack inversion symmetry, such as various 2D layered materials, and is widely used to characterize their properties.^[24–26,29,30] Furthermore, SHG has been combined with microscopy techniques enabling imaging of 2D materials. In this context, P-SHG imaging has been recently demonstrated as a powerful tool to probe the properties of 2D group VI transition metal dichalcogenides (TMDs), such as MoS₂, WS₂, MoSe₂, and WSe₂.^[31–37] Specifically, it has enabled direct optical imaging of the atomic edges and boundaries of a 2D material, based on the observation of electronic structure changes at the edges of monolayer MoS₂.^[31]

1. Introduction

Group IV monochalcogenides, also known as group IV–VI metal monochalcogenides, and denoted by MX with M = Sn, Ge and X = S, Se, are a class of layered, orthorhombic, semiconducting 2D materials attracting significant interest.^[1–3] They are known

G. M. Maragkakis, S. Psilodimitrakopoulos, L. Mouchliadis, A. S. Sarkar, A. Lemonis, G. Kioseoglou, E. Stratakis
Institute of Electronic Structure and Laser
Foundation for Research and Technology-Hellas
Heraklion Crete 71110, Greece
E-mail: stratak@iesl.forth.gr

G. M. Maragkakis, E. Stratakis
Department of Physics
University of Crete
Heraklion Crete 71003, Greece

G. Kioseoglou
Department of Materials Science and Technology
University of Crete
Heraklion Crete 71003, Greece

 The ORCID identification number(s) for the author(s) of this article can be found under <https://doi.org/10.1002/adom.202102776>.

DOI: 10.1002/adom.202102776

Furthermore, it has been used to calculate and map in a pixel-by-pixel manner the main crystallographic direction (armchair) of 2D TMDs,^[31–33] and quantify their crystal quality,^[32,33] determine the twist-angle in TMD homobilayers,^[34,35] and heterobilayers,^[36] and probe the valley population imbalance.^[37]

In this work, we extend the use of the P-SHG microscopy technique in order to investigate the properties of the orthorhombic 2D MXs. The 2D MXs are characterized by broken inversion symmetry, a fact that renders them suitable for SHG conversion.^[12–15] Indeed, using first-principles electronic structure theory, Wang and Qian theoretically predicted giant optical SHG in monolayer MXs.^[13] They predicted that the strength of SHG susceptibility of GeSe and SnSe monolayers is more than one order of magnitude higher than that of monolayer MoS₂. These results were also supported by another theoretical work by Panday and Fregoso.^[14] Recently, Higashitarumizu et al. performed polarized SHG spectroscopy on a micrometer-size monolayer SnS,^[12] while Zhu et al. reported anisotropic SHG in few-layer SnS.^[15]

The P-SHG methodology applied here is based on high-resolution P-SHG imaging microscopy, with spatial resolution of ≈500 nm (see Experimental Section). The subsequent fitting of the P-SHG polar diagrams for every pixel of the image with a theoretical model that accounts for the orthorhombic crystal structure of MXs, enables the calculation of the AC/ZZ direction from every point of a 2D SnS flake and the estimation of two ratios of the second-order nonlinear optical susceptibility tensor elements. We perform the same procedure for several different 2D SnS crystal flakes within the same field of view. It is shown that the mean and the standard deviation of the spatial distributions of the acquired values provide new means of contrast capable to discriminate 2D SnS crystals in the same image based on their in-plane structural anisotropy. Therefore, our technique provides insight into the nonlinear optical properties of 2D MXs and can serve as a useful characterization tool for emerging applications.

2. Results and Discussion

2.1. Theoretical Formulation of SHG from Orthorhombic MXs

In order to describe the interaction of an excitation field with a 2D orthorhombic MX crystal (Figure 1a) and the subsequent production of SHG, we use the Jones formalism.^[32–38] The two coordinate systems considered are schematically shown in Figure 1b: the laboratory frame (X, Y, Z) and the crystal coordinates (x, y, z), where z // Z. The laser beam propagates along Z axis, normally incident on the crystal, and linearly polarized along the sample plane, at an angle φ with respect to X laboratory axis. By rotating the half-waveplate, we vary the orientation of the excitation linear polarization, and record the SHG emerging from the sample as function of the polarization angle φ . The x axis is taken parallel to the ZZ direction of the crystal and at angle θ from X. The y direction is then along the AC crystallographic direction, which coincides with the mirror symmetry axis (Figure 1a).

The excitation field after passing the half-wave retardation plate can be expressed in laboratory coordinates by the Jones vector $\begin{pmatrix} E_0 \cos \varphi \\ E_0 \sin \varphi \end{pmatrix}$, where E_0 is the amplitude of the electric field. The expression of this vector in crystal coordinates is given by multiplying with the rotation matrix $\begin{pmatrix} \cos \theta & \sin \theta \\ -\sin \theta & \cos \theta \end{pmatrix}$, giving $E^\omega = \begin{pmatrix} E_0 \cos(\varphi - \theta) \\ E_0 \sin(\varphi - \theta) \end{pmatrix}$.

The 2D MXs belong to the non-centrosymmetric, orthorhombic point group C_{2v} (mm2).^[13] Thus, they have five independent, nonzero SHG susceptibility tensor elements, namely: $\chi_{yx}^{(2)}$, $\chi_{yy}^{(2)}$, $\chi_{yz}^{(2)}$, $\chi_{yx}^{(2)} = \chi_{xy}^{(2)}$, and $\chi_{zy}^{(2)} = \chi_{yz}^{(2)}$, where $\chi_{ijk}^{(2)}$ is the second-order nonlinear optical susceptibility tensor element along the different directions.^[13] As a result, the nonlinear polarization can be written in matrix form as:^[17]

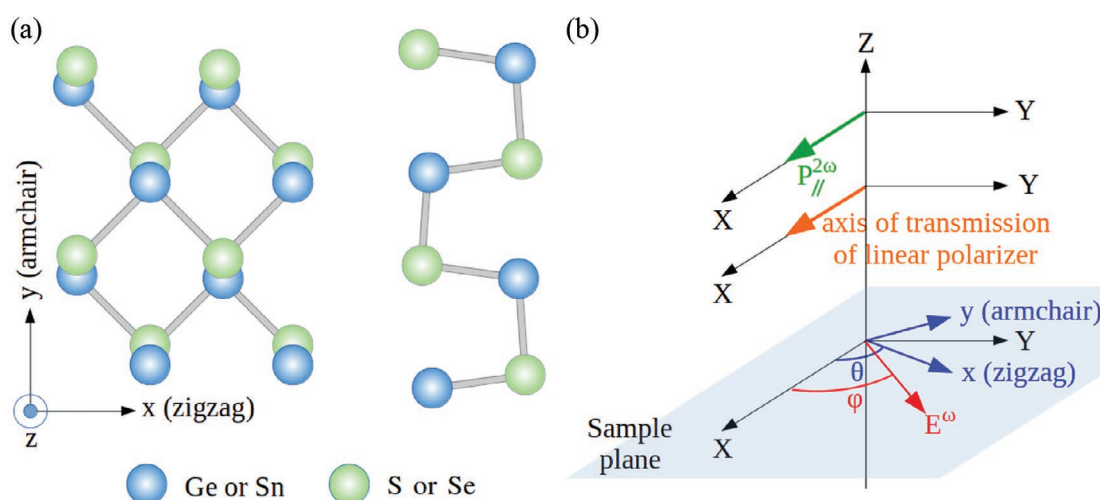


Figure 1. a) Schematic of the crystal structure of orthorhombic 2D MXs, as seen from the top (left) and the side (right). b) Illustration of the two coordinate systems, the laboratory X, Y, Z, and the crystal x, y, Z, adopted in our experimental configuration. The angles φ and θ describe the orientation of the laser field E^ω and the ZZ crystallographic direction relative to the X laboratory axis, respectively. $P_{\parallel}^{2\omega}$ shows the detected component of the generated SHG field.

$$\begin{pmatrix} P_x^{2\omega} \\ P_y^{2\omega} \\ P_z^{2\omega} \end{pmatrix} = \epsilon_0 \begin{pmatrix} 0 & 0 & 0 & 0 & 0 & \chi_{xy}^{(2)} \\ \chi_{yx}^{(2)} & \chi_{yy}^{(2)} & \chi_{yz}^{(2)} & 0 & 0 & 0 \\ 0 & 0 & 0 & \chi_{zy}^{(2)} & 0 & 0 \end{pmatrix} \begin{pmatrix} E_x^\omega E_x^\omega \\ E_y^\omega E_y^\omega \\ E_z^\omega E_z^\omega \\ 2E_x^\omega E_z^\omega \\ 2E_x^\omega E_y^\omega \\ 2E_y^\omega E_z^\omega \end{pmatrix} \quad (1)$$

where ϵ_0 is the permittivity of the free space. Given that the excitation field is polarized along the sample plane, we have considered $E_z^\omega = 0$, and thus the SHG equation is reduced to:

$$\begin{pmatrix} P_x^{2\omega} \\ P_y^{2\omega} \end{pmatrix} = \epsilon_0 E_0^2 \begin{pmatrix} \chi_{xy}^{(2)} \sin[2(\varphi - \theta)] \\ \chi_{yx}^{(2)} \cos^2(\varphi - \theta) + \chi_{yy}^{(2)} \sin^2(\varphi - \theta) \end{pmatrix} \quad (2)$$

where terms including only three independent SHG susceptibility tensor elements survive. We then transform this expression back to laboratory coordinates. In order to account for the effect of the linear polarizer placed before the detector, we multiply the SHG field with the Jones matrix $\begin{pmatrix} \cos^2 \zeta & \sin \zeta \cos \zeta \\ \sin \zeta \cos \zeta & \sin^2 \zeta \end{pmatrix}$, where ζ is the angle between the transmission axis of the polarizer and the X laboratory axis. In this work, we have set $\zeta = 0$, i.e., the axis of transmission of the polarizer parallel to X axis, and we measure the corresponding component of the SHG response, $P_{||}^{2\omega}$, whose intensity $I_{||}^{2\omega}$ is calculated as:

$$I_{||}^{2\omega} \sim \frac{1}{16} \left[2(\chi_{yx}^{(2)} + \chi_{yy}^{(2)}) \sin \theta + (2\chi_{xy}^{(2)} - \chi_{yx}^{(2)} + \chi_{yy}^{(2)}) \sin(\theta - 2\varphi) + (2\chi_{xy}^{(2)} + \chi_{yx}^{(2)} - \chi_{yy}^{(2)}) \sin(3\theta - 2\varphi) \right]^2 \quad (3)$$

In this relationship, the SHG intensity is expressed in terms of the absolute values of the $\chi^{(2)}$ tensor elements. Instead, we can express it in terms of dimensionless ratios of the $\chi^{(2)}$ tensor elements, obtaining:

$$I_{||}^{2\omega} = a \left[2(b+1) \sin \theta + (2c-b+1) \sin(\theta - 2\varphi) + (2c+b-1) \sin(3\theta - 2\varphi) \right]^2 \quad (4)$$

where

$$b = \chi_{yx}^{(2)} / \chi_{yy}^{(2)}, \quad c = \chi_{xy}^{(2)} / \chi_{yy}^{(2)} \quad (5)$$

and $a = \epsilon_0^2 E_0^4 / [16(\chi_{yy}^{(2)})^2]$ is a multiplication factor. The SHG intensity can also be expressed in the following equivalent form, which is used to fit the P-SHG experimental data:

$$I_{||}^{2\omega} = a \left[2(b+1) \sin \theta + (b-1) \left[(e-1) \sin(\theta - 2\varphi) + (e+1) \sin(3\theta - 2\varphi) \right] \right]^2 \quad (6)$$

where

$$e = 2c / (b-1) \quad (7)$$

In **Figure 2**, we present the numerical simulation of the $I_{||}^{2\omega}$ modulation, described by Equation (4), in polar plots, as function of the orientation of the linear polarization of the excitation field, φ , for fixed values of b, c , and for different AC/ZZ directions. A video presenting the P-SHG polar diagrams with a step of 10° in the ZZ direction θ is shown in Supporting Information. Remarkably, the shape of the polar diagram itself is predicted to change for different values of the AC/ZZ directions. Three possible shapes are obtained: one with four symmetric lobes, one with four lobes symmetric in pairs, and one with two symmetric lobes. This shape change is in contrast to the corresponding behavior of the P-SHG polar diagrams of monolayer TMDs, which belong to the D_{3h} point symmetry group, for which the $\chi^{(2)}$ tensor exhibits only one independent element.^[32,33] In that case, we have observed a characteristic four-lobe pattern, which rotates for different values of the crystal armchair direction (see also Video S2, Supporting Information).

The changes in the shape of the P-SHG polar diagrams, shown in **Figure 2**, reflect the in-plane anisotropy of the orthorhombic MXs. Indeed, the origin of this shape change is described by Equation (6), where the SHG intensity depends on four parameters, i.e., a, b, c , and θ . We are therefore able

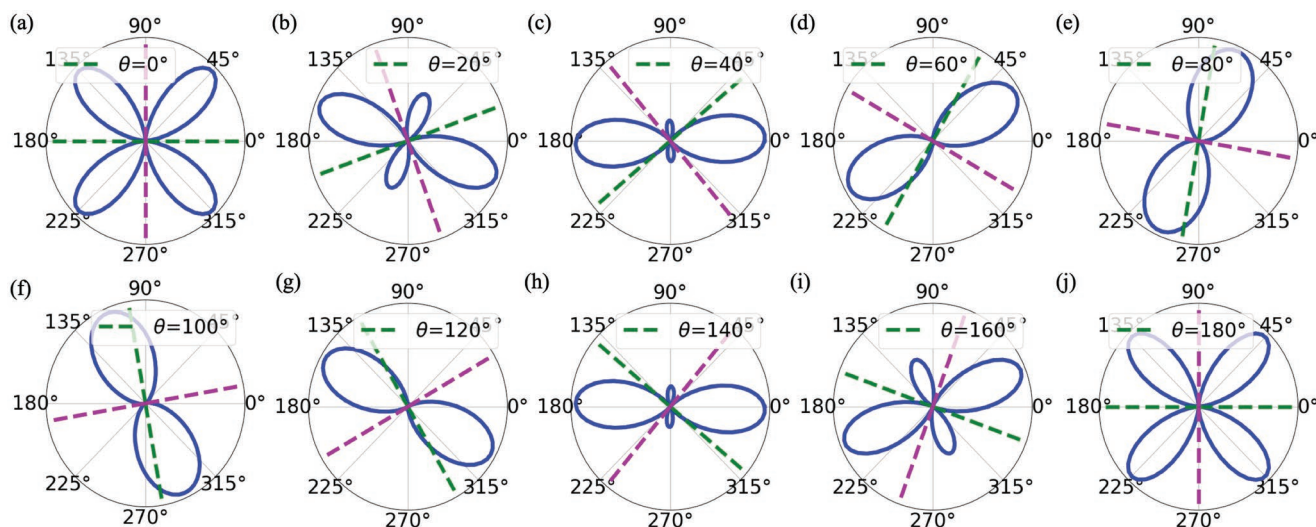


Figure 2. Numerical simulations of the theoretical P-SHG intensity produced by a 2D MX, described by Equation (4). We plot $I_{||}^{2\omega}$ in polar diagrams, as function of the orientation of the linearly polarized excitation angle φ for fixed values $b = 5, c = 6.5$, and for different ZZ directions θ , with $\theta \in [0^\circ, 180^\circ]$ with step 20° . The AC/ZZ directions are illustrated with the magenta/green lines for each case.

to establish a direct link between the P-SHG intensity modulation and the in-plane anisotropy of orthorhombic MXs through these four parameters. In particular, the shape of the theoretically predicted P-SHG polar diagrams shown in Figure 2 is determined by the ZZ direction θ and the tensor elements ratios b and c . The parameters b and c (Equation (5)) denote the relative contribution of different directions to the SHG signals. In Figures S1 and S2 (Supporting Information) we simulate the effect of different values of the $\chi^{(2)}$ element ratios b and c on the P-SHG polar diagrams.

In contrast to the monolayer TMDs where the AC direction can be calculated modulo 60° (due to their threefold rotational symmetry, i.e., the fact that they have three equivalent AC axes), in the case of 2D MXs, the AC direction is unique. This is readily reflected in the SHG polar diagrams of MXs which are the same every 180° in the AC/ZZ direction.

To describe the SHG intensity generated from an ultrathin orthorhombic 2D MX, with N number of layers with AA stacking sequence, we extend the interference model introduced for 2D TMDs.^[34,39] Neglecting propagation effects, the second harmonic field arising will have the form of vector superposition:

$$\mathbf{E}^{2\omega} = \mathbf{E}_1^{2\omega} + \mathbf{E}_2^{2\omega} + \dots + \mathbf{E}_N^{2\omega} \quad (8)$$

where the indices denote the second harmonic signal from the corresponding layers. The total SHG intensity produced by the N -layer structure, will then be:

$$I^{2\omega} = |\mathbf{E}_1|^2 + |\mathbf{E}_2|^2 + \dots + |\mathbf{E}_N|^2 + 2\mathbf{E}_1 \cdot \mathbf{E}_2 + \dots + 2\mathbf{E}_{N-1} \cdot \mathbf{E}_N \quad (9)$$

$$I^{2\omega} = I_1 + I_2 + \dots + I_N + 2\sqrt{I_1 I_2} \cos \delta_{1,2} + \dots + 2\sqrt{I_{N-1} I_N} \cos \delta_{N-1,N} \quad (10)$$

where $\delta_{i,j}$, $i, j = 1, 2, \dots, N$ denote the relative angle between layers i and j , i.e., the twist-angles, and the frequency index 2ω is suppressed for simplicity. If we assume for simplicity that the SHG intensity from the individual layers is equal ($I_1 = I_2 = \dots = I_N = I_{ML}$) and that the three layers are aligned (i.e., all twist-angles are zero), we find that

$$I^{2\omega} = NI_{ML} + I_{ML}N(N-1) \quad (11)$$

$$I^{2\omega} = N^2 I_{ML} \quad (12)$$

This is the well-known result that the SHG intensity from 2D flakes with zero twist-angle scales quadratically with the number of layers. It is valid for ultrathin non-centrosymmetric SnS with AA stacking sequence, where each layer contributes constructively in the detected SHG.

2.2. Nonlinear Imaging of In-Plane Anisotropy in SnS

Using our custom-built polarization-resolved nonlinear microscope presented in Figure 3, we raster-scan a specific sample area, and by rotating the linear polarization angle of the pump beam, φ , with a step of 2° , we record 180 spatially resolved images of $I_{ij}^{2\omega}$. We then fit these images with Equation (6) and estimate: i) the ZZ direction θ (and thus the perpendicular AC

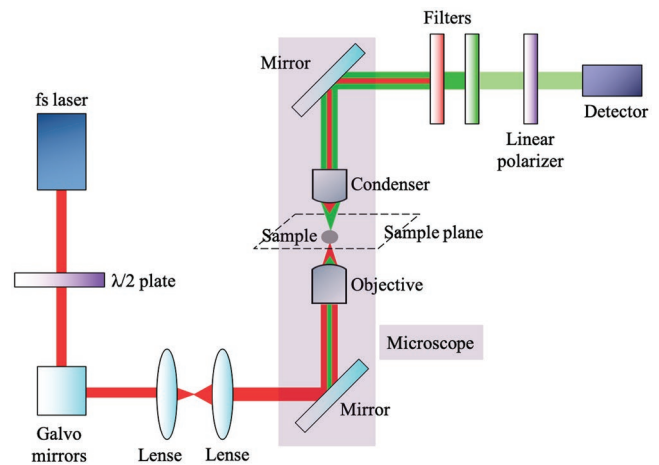


Figure 3. Illustration of the experimental setup. The fs laser beam is guided into the microscope and excites SHG produced by a stationary 2D SnS crystal. By rotating a $\lambda/2$ plate, we rotate the orientation of the linear polarization of the excitation field, as a function of which we record the second harmonic signal. A pair of galvanometric mirrors is used to raster-scan an area of the sample and obtain SHG images. The setup is discussed in detail in Experimental Section.

direction too); ii) the $\chi^{(2)}$ tensor element parameters b and c ; and iii) the multiplication factor a . This is performed for every pixel of the image enabling the extraction of spatially resolved images of the ZZ crystal direction and the tensor element parameters, as well as the corresponding distributions of their values.

In order to confirm the SHG process, we measure the average SHG intensity produced by a 2D SnS flake as function of the excitation power, shown in Figure S5 (Supporting Information) in a log-scale plot. Indeed, we obtain a quadratic power-law dependence, as expected. In Figure 4, we present representative P-SHG images of different 2D SnS crystals, belonging in the same field of view, for several orientations of the laser linear polarization φ denoted by the red arrow. A video of all the 180 P-SHG images obtained, with $\varphi \in [0^\circ, 360^\circ]$ with step 2° , can be found in the Supporting Information. A number of SnS flakes, appearing as bright spots of submicron dimensions, is observed. Six regions of interest (ROIs) containing SnS crystals are illustrated by the white arrows. While changing φ , we observe differences in the SHG intensity of the individual SnS flakes, in accordance with the theoretical predictions of Equations (4) and (6). We also note that the detected SHG signals from the different flakes are modulating out of phase. This is due to the different AC/ZZ crystallographic orientations and/or due to differences in the tensor element ratios among the different SnS flakes.

We focus on the six ROIs containing SnS crystals, illustrated by white arrows in Figure 4. In Figure 5a, we present for such ROIs the sum of the 180 P-SHG intensity images for all orientations of the excitation linear polarization φ . In Figure 5b–g, we present polar plots of the P-SHG modulation (in red dots) taken from one pixel inside the ROIs depicted in Figure 5a. These modulations agree with the mean and the integrated P-SHG modulation of each ROI (see Figure S6, Supporting Information for two representative examples). We note that the diagrams in Figure 5b–g confirm the theoretical prediction that

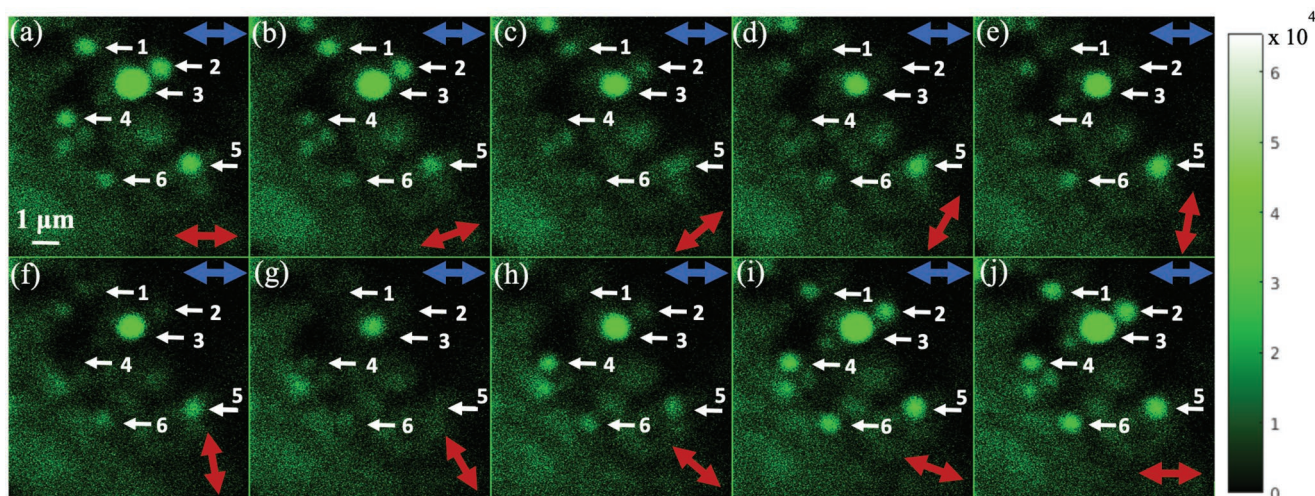


Figure 4. Experimental P-SHG images of ultrathin SnS crystals belonging in the same field of view for different values of the orientation of the laser linear polarization (φ in Equation (4)), denoted by the red arrows, with $\varphi \in [0^\circ, 180^\circ]$ with step 20° . The blue arrows indicate the direction of the polarization of the detected SHG signals. Brighter color indicates higher P-SHG intensity in arbitrary units. We note that the SHG signals from the 2D SnS crystals (ROIs 1–6 pointed by the white arrows), are modulating out of phase. The scale bar in the first image illustrates $1 \mu\text{m}$.

different SnS flakes can produce P-SHG polar plots of different shape (see Figure 2), depending on the ZZ crystallographic direction and the parameters b and e . Using our methodology, this is observed within the same field of view, providing new means of contrast. The third possible shape of the P-SHG polar diagrams, with two lobes as theoretically predicted in

Figure 2d–g, has also been experimentally demonstrated for another SnS flake and is presented in Figure S3 (Supporting Information). By fitting (blue line) the experimental data with Equation (6), we are able to calculate the AC/ZZ crystallographic direction and the $\chi^{(2)}$ element ratios, i.e., parameters b and c for each pixel (summarized in Table 1).

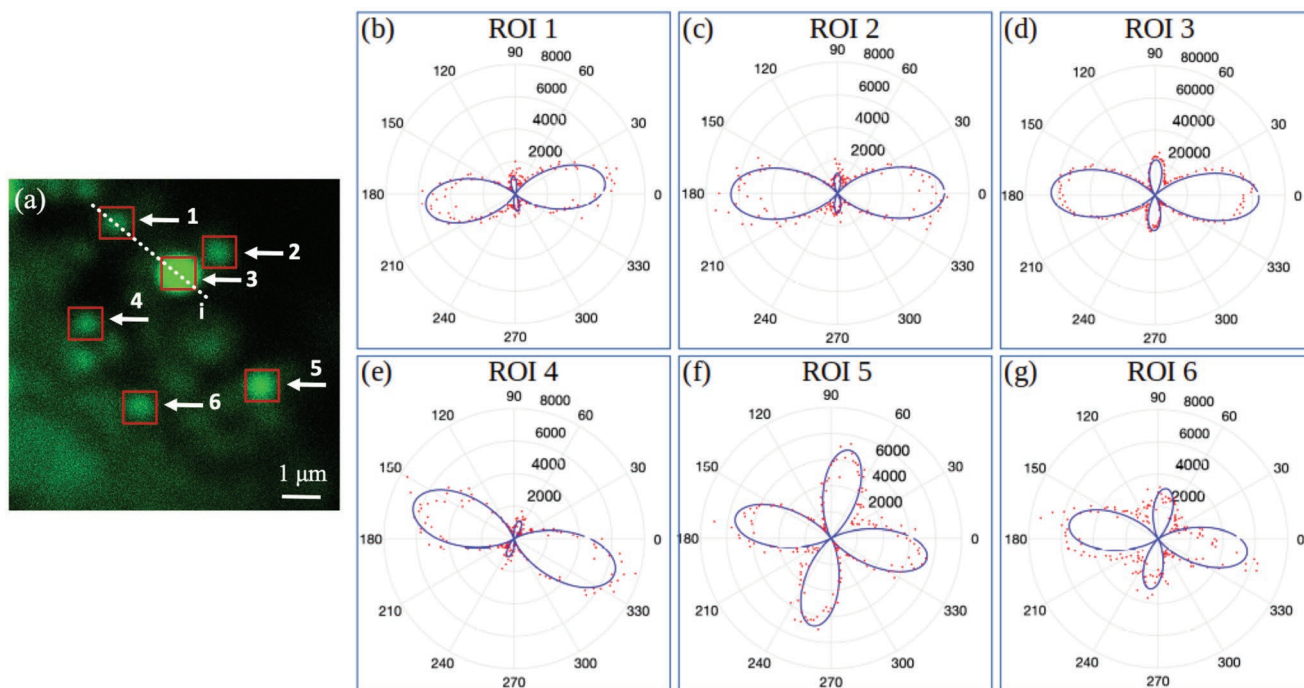


Figure 5. a) Sum of the SHG intensity for all orientations of the linearly polarized excitation angle φ , corresponding to the same field of view shown in Figure 4. Brighter color indicates higher SHG intensity. The scale bar illustrates $1 \mu\text{m}$. b–g) Experimental data (in red dots) of the P-SHG intensity taken from one pixel inside each ROI depicted in (a), presented in polar plots as function of the angle φ . By fitting (blue line) with Equation (6), we are able to calculate the ZZ crystallographic direction and the tensor element parameters b and e , for each pixel (summarized in Table 1). Interestingly, the shape of the polar diagrams changes for different flakes, which is the signature of differences in their in-plane anisotropy.

Table 1. Summary of the fitted parameters θ , a , b , and e , for all datasets demonstrated in Figure 5b–g, with the corresponding quality of fitting R^2 . The $\chi^{(2)}$ parameter c is calculated through Equation (7).

ROI	Zigzag direction θ [°]	Parameter a [arb. units]	Parameter $b = \chi_{yx}^{(2)}/\chi_{yy}^{(2)}$	Parameter $e = 2c/(b-1)$	Quality of fitting R^2	Parameter $c = \chi_{xy}^{(2)}/\chi_{yy}^{(2)}$
1	-33.96	2.78	5.05	7.33	85%	14.84
2	-40.35	2.57	6.16	7.15	92%	18.45
3	40.76	2.29	16.34	8.55	91%	65.58
4	23.67	2.56	9.09	3.75	91%	15.17
5	29.25	0.30	13.05	3.77	73%	22.71
6	29.36	0.91	12.59	3.07	56%	17.79

This fitting can also be performed in a pixel-by-pixel manner, producing spatially resolved ZZ orientation maps. Such maps along with their corresponding image histograms are presented in **Figure 6**, for the ROIs 1, 4–6 depicted in Figure 5a. Although, to date, only micrometer-size SnS monolayers have been realized, our technique can provide useful information on crystal quality and the presence of grain boundaries and defects in larger-area crystals.^[32,33] Using the same fitting procedure, we additionally produce distributions of values (image histograms) for the $\chi^{(2)}$ tensor element parameters b and e , which are presented in **Figure 7**. All such histograms are subsequently fitted with a Gaussian function in order to calculate the mean and standard deviation of the distribution of values for each parameter. **Table 2** summarizes the results of the fitted parameters θ , b , and e (mean and sigma), along with the values of c , calculated through Equation (7). Considering the broad range of the b , c , and e values, the results listed in Table 2 provide experimental and quantitative evidence on the highly anisotropic nature of the $\chi^{(2)}$ tensor of SnS.

To compare our findings with the literature, we use the values of the $\chi^{(2)}$ tensor elements of monolayer MXs that have been theoretically calculated from first-principles using density functional theory.^[13] For the particular case of SnS and for excitation pulse centered at 1028 nm ($\hbar\omega \approx 1.2$ eV), they have been calculated to be $\chi_{yy}^{(2)} \approx 65 \cdot 10^4 \text{ pm}^2 \text{ V}^{-1}$, $\chi_{yx}^{(2)} \approx 50 \cdot 10^4 \text{ pm}^2 \text{ V}^{-1}$, $\chi_{yy}^{(2)} \approx 10 \cdot 10^4 \text{ pm}^2 \text{ V}^{-1}$ (see Figure S2d, Supporting Information, Ref. [13]). These values correspond to $b = \chi_{yx}^{(2)}/\chi_{yy}^{(2)} \approx 5$, $c = \chi_{xy}^{(2)}/\chi_{yy}^{(2)} \approx 6.5$, $e = 2c/(b-1) \approx 3.25$, which agree with the experimental evidence that c is higher than b , while such values are within the same order of magnitude with the experimental values of Table 2. The deviations from the literature values, the broad histograms, and the different values of the $\chi^{(2)}$ parameters among different 2D SnS crystals may be attributed to i) deformation in the crystal lattice during the sample preparation,^[16] ii) varying contributions to the SHG signal from the $\chi^{(2)}$ tensor elements along different directions, and iii) the adopted fitting procedure. To our knowledge, there is only one work in which the authors have experimentally calculated relative magnitudes of the $\chi^{(3)}$ (instead of the $\chi^{(2)}$) tensor of a MX (few-layer GeSe).^[16] In that work, the authors have also reported deviations among different flakes, which they have possibly attributed to deformation in the crystal lattice during the exfoliation process. Such phenomenon has also been observed in the anisotropic third harmonic generation in exfoliated black phosphorus flakes.^[40]

We have also investigated the reason behind the considerably higher SHG intensity exhibited by one SnS flake (ROI 3) compared to its neighboring ones, as illustrated in Figures 4 and 5a. We note that the integrated SHG intensity from each SnS flake shown in Figure 5a (sum of all SHG intensities acquired for all the different excitation polarizations $\varphi \in [0^\circ, 360^\circ]$ with step 2°) is not polarization dependent anymore, and thus differences in

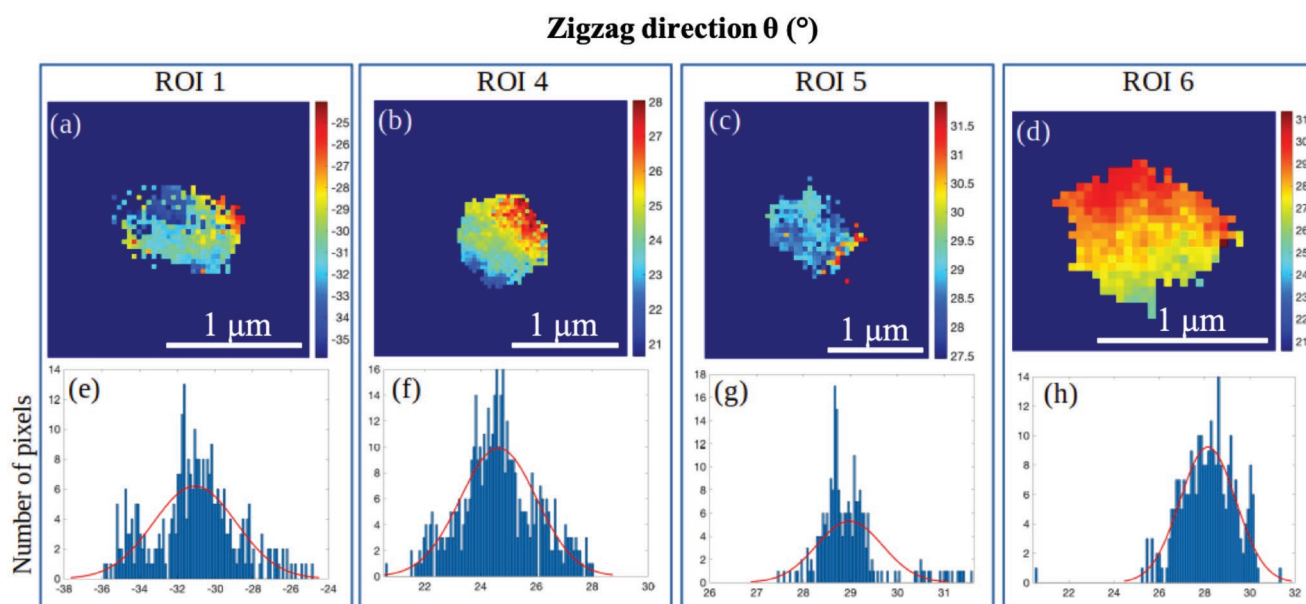


Figure 6. a–d) Pixel-by-pixel spatially resolved mapping of the ZZ crystallographic direction θ for the ultrathin SnS crystals which correspond to the ROIs 1, 4–6 depicted in Figure 5a. We present pixels that survived quality of fitting larger than 80%, 88%, 67%, and 50%, respectively. e–h) Corresponding image histograms showing the distributions of the values of the ZZ directions and the Gaussian fit (red line). The fitted parameters of the Gaussian fit are summarized in Table 2.

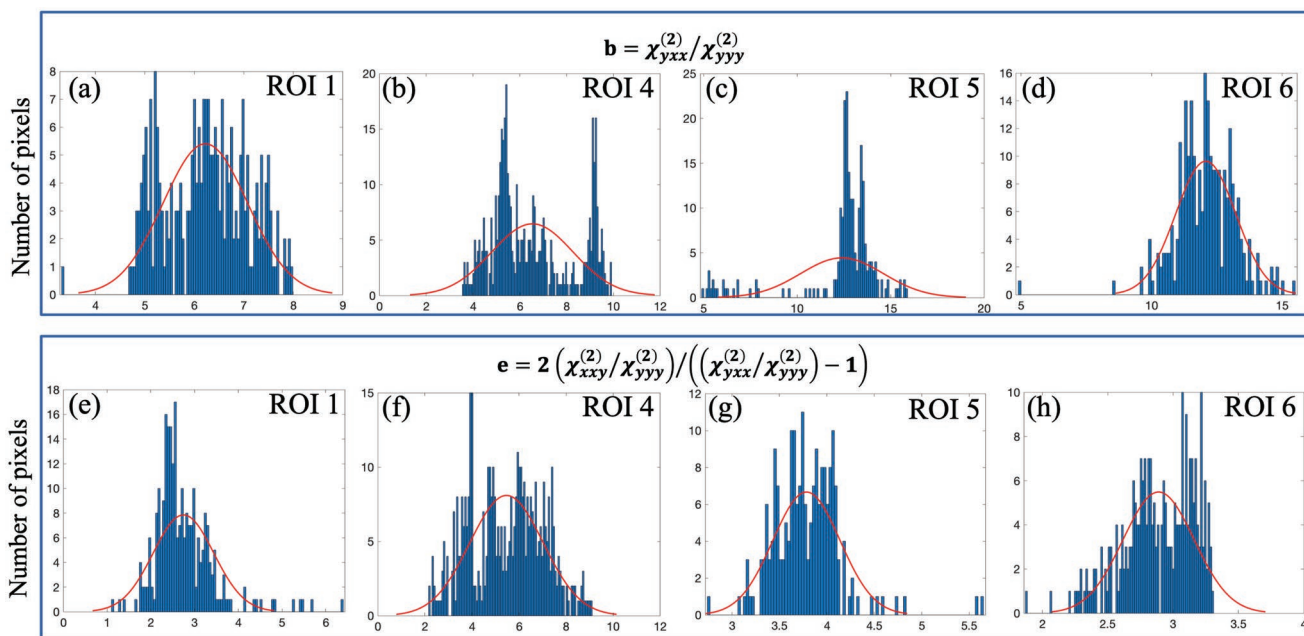


Figure 7. a–d) Histograms of the fitted $\chi^{(2)}$ parameter b (Equation (5)), and e–h) the fitted $\chi^{(2)}$ parameter e (Equation (7)), for the ultrathin SnS crystals which correspond to the ROIs 1, 4–6 depicted in Figure 5a. We present pixels that survived quality of fitting larger than 80%, 88%, 67%, and 50%, respectively. The fitted parameters of the Gaussian fit (red line) are summarized in Table 2.

the SHG intensities between the different flakes in the same image could solely be attributed to differences in their number of layers. In order to quantify these differences, Table 3 summarizes the maximum SHG intensities detected in each ROI. We characterized as monolayer the flake with the minimum intensity, i.e., ROI 1. The number of layers N for the other flakes is then determined using Equation (12) ($N = \sqrt{I/I_{ML}}$). We note that ROIs 2, 4–6 could also be characterized as monolayers. Interestingly, the intensity in these ROIs exhibits a variation. This variation may be attributed to the solvent overlayer, which could change the z -positions of the SnS crystals and place them slightly out of focus. This solvent residual is known to affect the measurement of the thickness of liquid phase exfoliated SnS flakes.^[45]

Here we try to address the thickness dependent SHG intensity in the 2D SnS crystals of our study by introducing a constructive interference model that describes the non-centrosymmetric AA stacking sequence of layered MX crystals

(Equation (12)). According to this model each layer contributes constructively in the detected SHG and the total SHG is analogous to N^2 , where N is the number of layers. However, like other MX compounds (GeS, GeSe, SnSe), a SnS crystal might also possess antiferroelectric order with alternating left and right polarization in the adjacent layers (i.e., the case of AB stacking sequence). In that case, the odd-layered crystals are non-centrosymmetric and provide SHG, while the bulk and even-layered crystals are usually centrosymmetric and should in principle not produce SHG signals.

In our experiments, we have found a SnS crystal (ROI 3) that produces nine times higher SHG signal than its surrounding crystals, as also shown in Figure 8, which presents the SHG intensity along the dashed line i shown in Figure 5a. The shape and magnitude of the polar diagram of ROI 3 (Figure 5d) fits well to the theoretical predictions of our constructive interference model (Equation (12)). This behavior (the N^2 times SHG

Table 2. Summary of the fitted parameters θ , b , and e (mean and standard deviation), based on the Gaussian fit illustrated in the representative histograms in Figures 6 and 7. The results for all ultrathin SnS crystals which correspond to the ROIs shown in Figure 5a are presented. The $\chi^{(2)}$ parameter c is calculated through the mean values of b and e using Equation (7).

ROI	Zigzag direction θ [°]		Parameter $b = \chi_{yxx}^{(2)}/\chi_{yyy}^{(2)}$		Parameter $e = 2c/(b - 1)$		Parameter $c = \chi_{xxy}^{(2)}/\chi_{yyy}^{(2)}$	
	Mean	Standard deviation	Mean	Standard deviation	Mean	Standard deviation	Mean	Standard deviation
1	−31.07	2.19	6.22	0.86	2.74	0.69	7.15	1.08
2	0.41	35.50	12.33	5.81	3.23	2.48	18.30	8.45
3	38.22	1.55	19.73	2.75	5.17	1.32	48.42	7.13
4	24.63	1.36	6.53	1.74	5.46	1.58	15.10	3.23
5	28.98	0.70	12.39	2.20	3.78	0.35	21.53	2.31
6	28.15	1.24	12.08	1.15	2.89	0.27	16.01	1.12

Table 3. Summary of the maximum SHG intensity detected from the ultrathin SnS crystals which correspond to the ROIs shown in Figure 5a. As monolayer is characterized the flake with the minimum intensity, i.e., ROI 1, while the number of layers N for the other flakes is determined using Equation (12).

ROI	Max. SHG intensity ($\times 10^5$) [arb. units]	Number of layers N
1	4.7	1
2	5.4	1.1
3	49	3.2
4	5.6	1.1
5	8.3	1.3
6	5.9	1.1

signal dependency) that appeared in our experimental data, could occur from a non-centrosymmetric, three-layer SnS crystal with AA stacking sequence.

3. Conclusion

In summary, taking advantage of the orthorhombic crystal structure of 2D SnS crystals that induces SHG conversion, we have optically mapped the in-plane optical anisotropy of 2D SnS flakes with high resolution. By performing P-SHG imaging microscopy, we found that the P-SHG polar plot changes shapes among different flakes. This finding reflects the effect of the in-plane anisotropy of the orthorhombic MXs on their nonlinear optical properties. This is demonstrated for different 2D SnS flakes belonging to the same field of view. Our approach provides new means of contrast that discriminates 2D SnS flakes in the same image based on their in-plane anisotropy. By fitting the experimental data with a nonlinear optics model, that accounts for the material crystal structure, we were able to calculate and map with high resolution the AC/ZZ crystallographic orientation of each flake, and to estimate two second-order

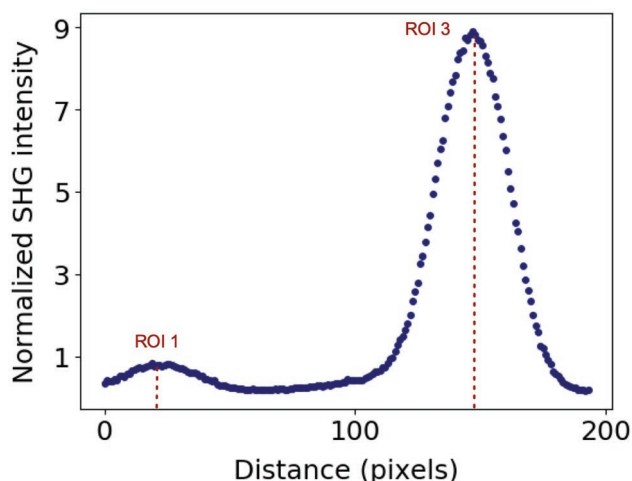


Figure 8. SHG intensity along the dashed line i shown in Figure 5a, normalized to the maximum intensity in ROI 1. The intensity in ROI 3 is found to be nine times higher than that of ROI 1, implying that ROI 3 could be a SnS trilayer.

nonlinear optical susceptibility tensor element ratios for every sample point. This methodology can be used to spatially determine in large crystal areas the optical in-plane anisotropy in different orthorhombic MXs crystals. Our results provide a novel, all-optical probe of the in-plane anisotropic properties of orthorhombic MXs based on nonlinear optics, that is useful for emerging fundamental studies and optoelectronic applications of these materials.

4. Experimental Section

Nonlinear Microscope: The experimental setup was based on an inverted microscope (Axio Observer Z1, Carl Zeiss), which uses a fs laser (FLINT FL1 Yb Oscillator, ≈ 6 W, 1028 nm, ≈ 76 MHz, ≈ 30 fs, Light Conversion) to pump nonlinear optical processes (Figure 3). A pair of silver-coated galvanometric (galvo) mirrors (6215H, Cambridge Technology) guided the laser beam into the microscope, allowing to raster-scan stationary samples. The beam passed through a zero-order half-wave retardation plate (QWPO-1030-10-2, CVI Laser), which was placed in a motorized rotation stage (M-060.DG, Physik Instrumente), with which the linear polarization of the excitation field with accuracy of 0.1° can be rotated. A pair of achromatic lenses suitably expanded the beam diameter to fill the back aperture of the objective lens (Plan-Apochromat $\times 40/1.3$ NA, Carl Zeiss).

At the motorized turret box of the microscope, there was an option of using either a silver mirror or a dichroic mirror, both at 45° just below the objective, depending on whether the produced signal was collected in the forward or backward (epi) detection geometry, respectively. In this work, the signal was collected in the forward direction, using the silver mirror which was insensitive to the laser beam polarization. The objective lens tightly focused the beam onto the stationary sample that produces SHG, which was collected by a condenser lens (achromatic-aplanatic, 1.4 NA, Carl Zeiss). Then, suitable short-pass (FF01-680/SP, Semrock) and narrow bandpass (FF01-514/3, Semrock) filters were used to cut off residual laser light and any other unwanted signal. Finally, a linear polarizer (LPVIS100-MP, ThorLabs) was placed before the detector which was based on a photomultiplier tube module (H9305-04, Hamamatsu), in order to select the detected SHG polarization.

The galvanometric mirrors and the photomultiplier tube were connected to a connector block (BNC-2110, National Instruments Austin), which was interfaced to a PC through a DAQ (PCI 6259, National Instruments). The coordination of the detector recordings with the galvanometric mirrors for the image formation, as well as the movement of the motors, was carried out using LabView (National Instruments).

This setup allowed to record spatially resolved SHG intensity images from a sample region, while rotating the linear polarization of the excitation field, performing P-SHG imaging. Each image (of 500×500 pixels in this work) corresponded to a sample area of size from a few μm to hundreds of μm , depending on how the movement of the galvo mirrors was set. The diffraction-limited spatial resolution was ≈ 500 nm ($0.61\lambda_{\text{exc}}/\text{NA}$, with $\text{NA} = 1.3$, $\lambda_{\text{exc}} = 1028$ nm). For the data analysis, the MATLAB (The Mathworks, Inc) programming language,^[41] the open-source Python programming language,^[42] and the open-source ImageJ image analysis software were used.^[43]

Sample Preparation and Characterization: The ultrathin layers of SnS sheets were isolated from bulk crystal via liquid phase exfoliation (LPE)^[44–46] (see Supporting Information). Figure S4a (Supporting Information) represents the UV–vis extinction spectra of isolated SnS sheets in acetone. The extinction spectra of SnS exhibited a broad absorption profile with UV–vis–NIR spectral range, accompanied with a shoulder at 420 nm. Such extinction spectral feature was consistent with the reported thin layers of SnS sheets,^[44–46] which suggested the isolation of an ultrathin layer of SnS sheets.

In addition, atomic force microscopy (AFM) images of isolated SnS were collected to acquire the flake dimensionality. As may be seen from

a representative area of the sample, shown in Figure S4b (Supporting Information), the height profile of each SnS sheet was varying, with all being less than ≈ 1.1 nm. It was noted that the ROIs 1–6 presented in Figure 4 did not correspond to the AFM profiles shown in Figure S4 (Supporting Information), which were from a representative area holding similar SnS flakes. Given that the monolayer SnS thickness is ≈ 0.6 nm and that AFM measurements of liquid phase exfoliated SnS have been reported to overestimate the thickness because of the solvent overlayer,^[45] the sample was identified to contain monolayers and bilayers.

Supporting Information

Supporting Information is available from the Wiley Online Library or from the author.

Acknowledgements

This research is co-financed by Greece and the European Union (European Social Fund-ESF) through the Operational Programme “Human Resources Development, Education and Lifelong Learning 2014–2020” in the context of the project “Crystal quality control of two-dimensional materials and their heterostructures via imaging of their non-linear optical properties” (MIS 5050340).

Conflict of Interest

The authors declare no conflict of interest.

Author Contributions

G.M.M. and S.P. contributed equally to this work. E.S. and G.K. guided the research. S.P. and G.M.M. conducted the optical experiments. G.M.M., L.M., and S.P. developed the theoretical model. S.P., G.M.M., L.M., and A.L. conducted the data analysis. A.S.S. prepared and characterized the samples. A.L. provided technical support. All authors contributed to the discussion and preparation of the manuscript.

Data Availability Statement

The data that support the findings of this study are available from the corresponding author upon reasonable request.

Keywords

2D materials, imaging microscopy, in-plane anisotropy, nonlinear optical properties, orthorhombic group-IV monochalcogenides, second harmonic generation, SnS

Received: December 20, 2021

Revised: February 17, 2022

Published online:

[1] A. S. Sarkar, E. Stratakis, *Adv. Sci.* **2020**, *7*, 2001655.

[2] F. Xia, H. Wang, J. C. M. Hwang, A. H. C. Neto, L. Yang, *Nat. Rev. Phys.* **2019**, *1*, 306.

- [3] L. Li, W. Han, L. Pi, P. Niu, J. Han, C. Wang, B. Su, H. Li, J. Xiong, Y. Bando, T. Zhai, *InfoMat* **2019**, *1*, 54.
- [4] L. C. Gomes, A. Carvalho, *Phys. Rev. B* **2015**, *92*, 085406.
- [5] H. Liu, A. T. Neal, Z. Zhu, Z. Luo, X. Xu, D. Tománek, P. D. Ye, *ACS Nano* **2014**, *8*, 4033.
- [6] A. Carvalho, M. Wang, X. Zhu, A. S. Rodin, H. Su, A. H. C. Neto, *Nat. Rev. Mater.* **2016**, *1*, 16061.
- [7] Z. Tian, C. Guo, M. Zhao, R. Li, J. Xue, *ACS Nano* **2017**, *11*, 2219.
- [8] Y. Yang, S.-C. Liu, Y. Wang, M. Long, C.-M. Dai, S. Chen, B. Zhang, Z. Sun, Z. Sun, C. Hu, S. Zhang, L. Tong, G. Zhang, D.-J. Xue, J.-S. Hu, *Adv. Opt. Mater.* **2019**, *7*, 1801311.
- [9] H. Yuan, X. Liu, F. Afshinmanesh, W. Li, G. Xu, J. Sun, B. Lian, A. G. Curto, G. Ye, Y. Hikita, Z. Shen, S.-C. Zhang, X. Chen, M. Brongersma, H. Y. Hwang, Y. Cui, *Nat. Nanotechnol.* **2015**, *10*, 707.
- [10] M. Wu, X. C. Zeng, *Nano Lett.* **2016**, *16*, 3236.
- [11] H. Wang, X. Qian, *2D Mater.* **2017**, *4*, 015042.
- [12] N. Higashitarumizu, H. Kawamoto, C.-J. Lee, B.-H. Lin, F.-H. Chu, I. Yonemori, T. Nishimura, K. Wakabayashi, W.-H. Chang, K. Nagashio, *Nat. Commun.* **2020**, *11*, 2428.
- [13] H. Wang, X. Qian, *Nano Lett.* **2017**, *17*, 5027.
- [14] S. R. Panday, B. M. Fregoso, *J. Phys.: Condens. Matter* **2017**, *29*, 43LT01.
- [15] M. Zhu, M. Zhong, X. Guo, Y. Wang, Z. Chen, H. Huang, J. He, C. Su, K. P. Loh, *Adv. Opt. Mater.* **2021**, *9*, 2101200.
- [16] A. Dasgupta, J. Gao, X. Yang, *Laser Photonics Rev.* **2020**, 1900416.
- [17] R. W. Boyd, *Nonlinear Optics*, Academic Press, Elsevier, San Diego, CA **2020**.
- [18] Y. R. Shen, *The Principles of Nonlinear Optics*, Wiley Press, New York, NY **1984**.
- [19] C. Li, *Nonlinear Optics, Principles and Applications*, Springer, Singapore **2017**.
- [20] G. New, *Introduction to Nonlinear Optics*, Cambridge University Press, Cambridge **2011**.
- [21] J. Leuthold, C. Koos, W. Freude, *Nat. Photonics* **2010**, *4*, 535.
- [22] D. E. Chang, V. Vuletic, M. D. Lukin, *Nat. Photonics* **2014**, *8*, 685.
- [23] M. Kauranen, A. V. Zayats, *Nat. Photonics* **2012**, *6*, 737.
- [24] A. Autere, H. Jussila, Y. Dai, Y. Wang, H. Lipsanen, Z. Sun, *Adv. Mater.* **2018**, *30*, 1705963.
- [25] X. Wen, Z. Gong, D. Li, *InfoMat* **2019**, *1*, 317.
- [26] L. Zhou, H. Fu, T. Lv, C. Wang, H. Gao, D. Li, L. Deng, W. Xiong, *Nanomaterials* **2020**, *10*, 2263.
- [27] D. Xydias, G. Ziakas, S. Psilodimitrakopoulos, A. Lemonis, E. Bagli, T. Fotsis, A. Gravanis, D. S. Tzeranis, E. Stratakis, *Biomed. Opt. Express* **2021**, *12*, 1136.
- [28] V. Tsafas, E. Gavgiotaki, M. Tzardi, E. Tsafa, C. Fotakis, I. Athanassakis, G. Filippidis, *J. Biophotonics* **2020**, *13*, e202000180.
- [29] Y. Wang, J. Xiao, S. Yang, Y. Wang, X. Zhang, *Opt. Mater. Express* **2019**, *9*, 1136.
- [30] H. Ma, J. Liang, H. Hong, K. Liu, D. Zou, M. Wu, K. Liu, *Nanoscale* **2020**, *12*, 22891.
- [31] X. Yin, Z. Ye, D. A. Chenet, Y. Ye, K. O'Brien, J. C. Hone, X. Zhang, *Science* **2014**, *344*, 488.
- [32] S. Psilodimitrakopoulos, L. Mouchliadis, I. Paradisanos, A. Lemonis, G. Kioseoglou, E. Stratakis, *Light: Sci. Appl.* **2018**, *7*, 18005.
- [33] G. M. Maragkakis, S. Psilodimitrakopoulos, S. L. Mouchliadis, I. Paradisanos, A. Lemonis, G. Kioseoglou, E. Stratakis, *Opto-Electron. Adv.* **2019**, *2*, 190026.
- [34] S. Psilodimitrakopoulos, L. Mouchliadis, I. Paradisanos, G. Kourmoulakis, A. Lemonis, G. Kioseoglou, E. Stratakis, *Sci. Rep.* **2019**, *9*, 14285.
- [35] S. Psilodimitrakopoulos, A. Orekhov, L. Mouchliadis, D. Jannis, G. M. Maragkakis, G. Kourmoulakis, N. Gauquelin, G. Kioseoglou, J. Verbeeck, E. Stratakis, *npj 2D Mater. Appl.* **2021**, *5*, 77.
- [36] S. Psilodimitrakopoulos, L. Mouchliadis, G. M. Maragkakis, G. Kourmoulakis, A. Lemonis, G. Kioseoglou, E. Stratakis, *2D Mater.* **2021**, *8*, 015015.

- [37] L. Mouchliadis, S. Psilodimitrakopoulos, G. M. Maragkakis, I. Demeridou, G. Kourmoulakis, A. Lemonis, G. Kioseoglou, E. Stratakis, *npj 2D Mater. Appl.* **2021**, 5, 6.
- [38] E. Hecht, *Optics*, Pearson Education Limited, Harlow, United Kingdom **2017**.
- [39] W.-T. Hsu, Z.-A. Zhao, L.-J. Li, C.-H. Chen, M.-H. Chiu, P.-S. Chang, Y.-C. Chou, W.-H. Chang, *ACS Nano* **2014**, 8, 2951.
- [40] A. Autere, C. R. Ryder, A. Säynätjoki, L. Karvonen, B. Amirsolaimani, R. A. Norwood, N. Peyghambarian, K. Kieu, H. Lipsanen, M. C. Hersam, Z. J. Sun, *J. Phys. Chem. Lett.* **2017**, 8, 1343.
- [41] D. J. Higham, N. J. Higham, *MATLAB Guide*, Siam, Philadelphia, PA **2016**.
- [42] G. van Rossum, Python tutorial, Technical Report CS-R9526, Centrum voor Wiskunde en Informatica (CWI), Amsterdam, May **1995**.
- [43] C. A. Schneider, W. S. Rasband, K. W. Eliceiri, *Nat. Methods* **2012**, 9, 671.
- [44] A. S. Sarkar, E. Stratakis, *J. Colloid Interface Sci.* **2021**, 594, 334.
- [45] J. R. Brent, D. J. Lewis, T. Lorenz, E. A. Lewis, N. Savjani, S. J. Haigh, G. Seifert, B. Derby, P. O'Brien, *J. Am. Chem. Soc.* **2015**, 137, 12689.
- [46] A. S. Sarkar, A. Mushtaq, D. Kushavah, S. K. Pal, *npj 2D Mater. Appl.* **2020**, 4, 1.